Onodera et al. *NPG Asia Materials* (2024) 16:22
https://doi.org/10.1038/s41427-024-00542-y

NPG Asia Materials

ARTICLE Open Access

# Formation of a zirconium oxide crystal nucleus in the initial nucleation stage in aluminosilicate glass investigated by X-ray multiscale analysis

Yohei Onodera[1,2], Yasuyuki Takimoto[3], Hiroyuki Hijiya[4], Qing Li[4], Hiroo Tajiri[5], Toshiaki Ina[6] and Shinji Kohara[1]

**Abstract**

Understanding the nucleation mechanism in glass is crucial for the development of new glass-ceramic materials. Herein, we report the structure of a commercially important glass-ceramic $ZrO_2$-doped lithium aluminosilicate system during its initial nucleation stage. We conducted an X-ray multiscale analysis, and this analysis was used to observe the structure from the atomic to the nanometer scale by using diffraction, small-angle scattering, absorption, and anomalous scattering techniques. The inherent phase separation between the Zr-rich and Zr-poor regions in the pristine glass was enhanced by thermal treatment without changing the spatial geometry at the nanoscale. Element-specific pair distribution function analysis using anomalous X-ray scattering data showed the formation of a liquid $ZrO_2$-like local structural motif and edge sharing between the $ZrO_x$ polyhedra and $(Si/Al)O_4$ tetrahedra during the initial nucleation stage. Furthermore, the local structure of the $Zr^{4+}$ ions resembled a cubic or tetragonal $ZrO_2$ crystalline phase and formed after 2 h of annealing the pristine glass. Therefore, the Zr-centric periodic structure formed in the early stage of nucleation was potentially the initial crystal nucleus for the Zr-doped lithium aluminosilicate glass-ceramic.

## Introduction

Glass-ceramics are composed of precipitated crystals and a glass matrix and are utilized in many industrial products, such as high-temperature furnace windows, cooktop panels, artificial teeth, and telescope mirrors[1,2]. These materials exhibit unique characteristics that are not observed in conventional glasses. For instance, several glass-ceramics exhibit high mechanical strength owing to the presence of encrusted crystals, which block crack propagation in a glass matrix. Glass-ceramics are synthesized by intentionally reheating quenched pristine glass above its glass transition temperature to obtain homogeneous crystallization. The properties of glass-ceramics are affected by various factors, such as the composition, shape and size of the crystals and crystallinity. Hence, these factors need to be controlled with high reproducibility to enable the practical use of glass-ceramics.

The addition of nucleation agents to the host glass is an effective method for producing glass-ceramics; nucleation agents aid and control the crystallization process[3]. Zirconium oxide ($ZrO_2$) is a commonly used nucleation agent that acts as the nucleation center for $ZrO_2$ microcrystals in various glass-ceramics[1–3]. Aluminosilicate ($Al_2O_3$–$SiO_2$) systems with $ZrO_2$ are the most important commercial glass-ceramics and are used in numerous optical and photonic applications owing to their low thermal expansion coefficients, high strengths, and high fracture toughness.

Several studies on pristine aluminosilicate glasses and glass-ceramics with $ZrO_2$ have been performed using a combination of X-ray diffraction (XRD), X-ray absorption

Correspondence: Yohei Onodera (ONODERA.Yohei@nims.go.jp) or Yasuyuki Takimoto (yasuyuki.takimoto@agc.com)
[1]Center for Basic Research on Materials, National Institute for Materials Science, 1-2-1 Sengen, Tsukuba, Ibaraki 305-0047, Japan
[2]Institute for Integrated Radiation and Nuclear Science, Kyoto University, 2-1010 Asashiro-nishi, Kumatori-cho, Sennan-gun, Osaka 590-0494, Japan
Full list of author information is available at the end of the article

spectroscopy (XAS), and transmission electron microscopy (TEM) to elucidate the local structure of $Zr^{4+}$ and the formation mechanism of nanocrystalline $ZrO_2$[4–8]. In the case of pristine glasses, Dargaud et al. reported that the $Zr^{4+}$ environment in $MgO–Al_2O_3–SiO_2–ZrO_2$ glass corresponded to a sevenfold coordinated site linked mainly with $SiO_4$ tetrahedra by edge sharing, according to the results from extended X-ray absorption fine structure (EXAFS) measurements at 77 K[4]. Patzig et al. used a combination of Zr $L_{II,III}$-edge X-ray absorption near edge structure (XANES), scanning TEM (STEM), and energy-dispersive X-ray spectroscopy and observed sixfold coordination around $Zr^{4+}$ in the $MgO–Al_2O_3–SiO_2–ZrO_2$ glass[5]. Moreover, they showed a transformation of the Zr coordination number from approximately six in pristine glass to eight after the completion of crystallization in $MgO–Al_2O_3–SiO_2–ZrO_2$ systems[5,6]. Conversely, Cormier et al. investigated the role of $ZrO_2$ in the nucleation of several aluminosilicate glasses by XAS at both Zr K- and $L_{II,III}$-edges. They indicated that the $Zr^{4+}$ environment corresponded to a sixfold coordinated site in Li- and Na-bearing glasses and that sevenfold coordinated sites are formed in Mg-, Ca-, and Zn-containing glasses[7]. Based on combined XANES and TEM results from the $Li_2O–Al_2O_3–SiO_2–ZrO_2$ glass-ceramics, Kleebusch et al. recently reported that the crystallization of nanoscale $ZrO_2$ occurred with a gradual change in the coordination state of $Zr^{4+}$ from sixfold in pristine glass to eightfold in the crystal[8].

The $Zr^{4+}$ environments in pristine glasses and sufficiently crystallized glass-ceramics have been studied using various experimental techniques. However, in glass-ceramics, the environment around the $Zr^{4+}$ ions in an intermediate state between the glass and crystals, particularly in the early stage of nucleation, is still not well understood. Structural modifications, for example, change in the coordination number around $Zr^{4+}$ and the formation process of the polyhedral connectivity of the $ZrO_x$ units at the early stage of nucleation, are crucial for further understanding the role of $Zr^{4+}$ in the nucleation process. In particular, determining the clustering process considering the connectivity of the $ZrO_x$ units is indispensable for understanding the origin of nucleation because the $ZrO_x$ clustering potentially triggers nucleation and occurs on an intermediate-range scale; this intermediate-range scale exists on a length scale larger than the nearest-neighbor distance. However, the conventional approach using XAFS is ineffective for investigating the intermediate-range ordering in oxide glasses owing to their structural disorders. The EXAFS signals are immediately damped beyond the nearest-neighbor distance, particularly for glasses[9]. Therefore, XAFS is unsuitable for elucidating intermediate-range structural ordering in glasses and glass-ceramics in the early stage of nucleation.

In contrast, pair distribution function (PDF) analysis is useful for probing short- to intermediate-range ordering in glasses. The PDF is obtained by the Fourier transform of the structure factor $S(Q)$, which is the normalized scattering intensity obtained from quantum beam (X-ray and neutron) diffraction measurements. PDF analysis provides the interatomic distances and average coordination numbers[10–12]. In several previous investigations, the PDF analysis with structural modeling techniques showed that the coordination number of a cation in a glass was different from that in a crystal[13–17]. For instance, Mg–O species adopted four, five, and six-coordination in silicate glass that contains insufficient network formers[13]; $ZnO_x$ (average $x < 4$) polyhedra formed the network in Zn-rich binary phosphate glass[15]; and K ions were trapped in highly coordinated K–O polyhedra, forming a correlated pair arrangement with Na–O polyhedra in silicate glass with the mixed alkali effect[16]. These cation coordination environments are characteristic of glasses and rarely derived solely by EXAFS because the EXAFS analysis of glassy materials is performed using a well-defined crystalline structure as a reference. Hence, PDF analysis is advantageous for investigating glass structures. However, extraction of the specific pair correlations, such as Zr-related correlations, from a PDF is challenging for multicomponent glasses and glass-ceramics (which mostly include four or more oxides to enable practical use) because the pair correlation peaks are greater than 10 atomic pairs in the PDF. Therefore, an element-specific technique based on diffraction is required to probe Zr-specific structural information beyond short-range ordering in practical glass-ceramics.

In this study, we examine lithium aluminosilicate glass and its glass-ceramic, which is a commercially important system due to its attractive properties, such as low/negative thermal expansion coefficients. A small amount of $ZrO_2$ (2.9 mol%) was added as a nucleation agent to the glass to crystallize the glass-ceramic. To investigate the structural ordering relative to the small amount of Zr in the glass and glass-ceramic at both short- and intermediate-range scales, we employed anomalous X-ray scattering (AXS) measurements. AXS utilizes anomalous variations in the atomic form factor of a specific element close to the X-ray absorption edge and provides element-specific structural information beyond the nearest-neighbor distance[18–21]. Therefore, the atomic distances and coordination numbers around Zr were determined by element-specific PDF analysis using the AXS data. The local structure of Zr was also studied using XAFS measurements. The XAFS spectra were measured using the Zr K-edge because K-edge XAFS measurements enabled the attainment of the EXAFS spectra up to a higher wavenumber ($k$) than those obtained using the L-edge. The XANES spectra were utilized to determine the valence state of Zr, and the EXAFS spectra were analyzed as a reference for element-specific PDF analysis. The combination of AXS and EXAFS has been

applied to studies of $CaO–SiO_2–ZrO_2$ glass-ceramics[22] and lithium germanate glasses[23] to investigate the local structural motifs of Zr or Ge atoms. Small-angle X-ray scattering (SAXS) is a useful method for probing inhomogeneity in materials when examining the phase separation of nanometer or submicrometer order. Therefore, SAXS was used to observe the behavior of the nanoscale structures during nucleation. In this study, lithium aluminosilicate glass-ceramics in the initial nucleation stage were prepared by thermal treatment of pristine glass. The nanoscale structures of the pristine glass and glass-ceramics were probed by combining SAXS with in-house XRD. The short-range structures of the pristine glass and glass-ceramics were analyzed using a combination of XAFS and AXS. Furthermore, the AXS data were investigated in both $Q$ and real spaces to determine the formation mechanism of the structural ordering, which was consistent with the SAXS results in the intermediate range in the early stage of nucleation. Thus, we performed a state-of-the-art multiscale structural analysis based on synchrotron X-ray experiments on Zr-doped lithium aluminosilicate glass and glass-ceramic materials. This novel approach demonstrates the behavior of a small number of Zr cations from the atomic scale to the nanoscale in the initial nucleation stage in commercially available glass-ceramic materials.

## Materials and methods

### Materials

Lithium aluminosilicate glass with small amounts of zirconium oxide, sodium oxide, and phosphorus pentoxide (pristine glass) was prepared using a conventional melt-quenching method. The raw materials in the prescribed amounts were sufficiently mixed and melted at 1650 °C for 12 h to achieve homogeneous melting. The material was then quenched and rapidly solidified to prevent partial crystallization. The chemical composition of the pristine glass is listed in Table 1. Large portions of the obtained glass pieces were cut and polished to a thickness of 1.2 mm for the subsequent experiments. The residual glass was crushed for thermal analysis. The pristine glass samples were annealed at a crystallization onset temperature determined by thermal analysis for several durations between 0 and 48 h to obtain glass-ceramic samples at different nucleation stages. The XRD measurements were performed using a Rigaku SmartLab diffractometer with an X-ray source of Cu Kα radiation to confirm the formation of amorphous and crystalline phases. The density of the pristine glass obtained using the Archimedean method was 2.55 g $cm^{-3}$; this value corresponded to a number density of 0.0759 $Å^{-3}$.

### Differential scanning calorimetry (DSC) measurement

DSC was performed to elucidate the crystallization behavior of the pristine glass during heating. A crushed glass sample was sifted to obtain glass particles with sizes ranging from 106 to 180 μm for DSC measurements. DSC was performed at a constant heating rate of 10 °C $min^{-1}$ using a DSC3300SA differential scanning calorimeter (Bruker, Inc.).

**Table 1 Glass composition.**

| Composition | mol% |
|---|---|
| $SiO_2$ | 70.7 |
| $Al_2O_3$ | 14.3 |
| $P_2O_5$ | 0.7 |
| $ZrO_2$ | 2.9 |
| $Li_2O$ | 9.3 |
| $Na_2O$ | 2.1 |
| Total | 100.0 |

### Synchrotron X-ray measurements

The SAXS measurements were performed using the BL8S3 beamline at the Aichi Synchrotron Radiation Center. The energy of the incident X-rays was 13.5 keV. The camera length was 2174.1 mm, and a two-dimensional detector (PILATUS 100 K) was used. The exposure time for each measurement was 480 s.

The Zr K-edge (18.01 keV) XAFS measurements were performed using the BL5S1 beamline at the Aichi Synchrotron Radiation Center by employing a Si(111) double-crystal monochromator in transmission mode. The obtained XAFS spectra were normalized and analyzed using Athena and Artemis software[24]. The $k^3$-weighted EXAFS spectra, $k^3\chi(k)$, were Fourier transformed (FT) over a $k$-range of 3.0–12.0 $Å^{-1}$ to obtain the radial structure functions. The Zr–O distances ($r_{Zr-O}$) and Zr–O coordination numbers ($N_{Zr-O}$) were determined by curve fitting the EXAFS data using Artemis software[24]. A fixed Debye–Waller factor of 0.009 Å2 was used; this value was obtained from the curve fitting to Zr K-edge EXAFS data for yttria-stabilized zirconia (YSZ) crystals.

The AXS measurements were performed using a dedicated AXS spectrometer[21] built at the BL13XU beamline[25,26] at the SPring-8 synchrotron radiation facility. The spectrometer consisted of a six-circle diffractometer, a vacuum sample chamber, receiving slits, a beam stop, a LiF analyzer crystal, and a NaI (Tl) scintillation detector. The energy resolution of the LiF(200) crystal was approximately 12 eV at the full width at half maximum at 12 keV, which enabled the discrimination of the contributions of fluorescence and Compton scattering. The AXS measurements were performed at two incident X-ray energies, 17.81 keV (Zr far edge, $E_{far}$) and 17.99 keV (Zr near edge, $E_{near}$); these were 200 eV and 20 eV below the Zr K-edge, respectively. The scattering intensities were collected using reflection geometry for 200 min for each

sample. The differential intensity ($\Delta_{Zr}I$) between two scattering intensities measured at $E_{far}$ and $E_{near}$ is expressed as follows:

$$\alpha\Delta_{Zr}I(Q,E_{far},E_{near}) = \Delta_{Zr}\left[\langle f(Q)^2\rangle - \langle f(Q)\rangle^2\right] + \Delta_{Zr}\left[\langle f(Q)\rangle^2\right]\Delta_{Zr}S(Q), \quad (1)$$

and

$$\langle f(Q)^2\rangle = \sum_i c_i f_i^2(Q), \quad (2)$$

$$\langle f(Q)\rangle^2 = \left(\sum_i c_i f_i(Q)\right)^2, \quad (3)$$

where $\alpha$ is a normalization constant, $\Delta_{Zr}[\quad]$ indicates the difference in values in the brackets at the energies of $E_{far}$ and $E_{near}$ of Zr, and $c_i$ and $f_i(Q)$ are the concentration and atomic form factor of the component atom $i$, respectively. The differential structure factor $\Delta_{Zr}S(Q)$ is given by a linear combination of the partial structure factors $S_{ij}(Q)$, as follows:

$$\Delta_{Zr}S(Q) = \sum_{i=1}^{N}\sum_{j=1}^{N} w_{ij}(Q,E_{far},E_{near})S_{ij}(Q), \quad (4)$$

where the weighting factors are given by the following:

$$w_{ij}(Q,E_{far},E_{near}) = c_i c_j \frac{\Delta_{Zr}\left[f_i(Q)f_j(Q)\right]}{\Delta_{Zr}\left[\langle f(Q)\rangle^2\right]}. \quad (5)$$

Compared with the total structure factor $S(Q)$ obtained from XRD, $\Delta_{Zr}S(Q)$ greatly enhances the contribution from Zr-related $S_{ij}(Q)$ and suppresses the contributions from the other partials. By approximating $f_i(Q)$ by using the atomic number, the weighting factors in the $\Delta_{Zr}S(Q)$ can be calculated as follows:

$$\Delta_{Zr}S(Q) = 0.033S_{ZrZr}(Q) + 0.312S_{ZrSi}(Q) + 0.117S_{ZrAl}(Q) + 0.018S_{ZrLi}(Q) + 0.015S_{ZrNa}(Q) + 0.521S_{ZrO}(Q), \quad (6)$$

where the weighting factors for the partials other than those mentioned above were almost zero; these partial structure factors were reasonably eliminated in $\Delta_{Zr}S(Q)$.

## Results and discussion

### Preparation of the glass-ceramic samples in the initial nucleation stage

The DSC curve of the pristine glass is shown in Fig. 1. Three broad exothermic maxima were observed at approximately 800, 860, and 1045 °C. The in-house XRD patterns of the samples annealed at different temperatures are shown in Fig. S1. In the XRD pattern of the sample annealed at 800 °C, several broad peaks were observed at approximately 30°, 35°, 50°, and 60° and were assigned to cubic (c-) or tetragonal (t-) $ZrO_2$. However, we could not distinguish between these two phases because the XRD peaks were extremely broad. Based on these results, the first exothermic peak in the DSC curve was assigned to the nucleation of c- or t-$ZrO_2$ in the pristine glass structure. The second and third exothermic peaks were assigned to the actual crystallization of the β-quartz solid solution (s.s.)[27] and the phase transition from β-quartz s.s. to β-spodumene s.s.[27], respectively. A slight baseline shift to the endothermic direction owing to the glass transition was observed at approximately 745 °C in the DSC curve. As shown in Fig. 1 and S1, the morphological change during annealing in pristine glass occurred in four steps: (i) a decrease in viscosity at the glass transition temperature, (ii) nucleation of the $ZrO_2$ crystal, (iii) crystallization of β-quartz s.s., and (iv) phase transition from β-quartz s.s. to β-spodumene s.s.

A series of glass-ceramic samples at different nucleation stages were synthesized to elucidate the structural changes around Zr during the nucleation process. By elucidating the results of the thermal treatments based on the DSC curve, an annealing temperature of 770 °C was found to be suitable; this temperature corresponded to the crystallization onset temperature. Based on this consideration, the pristine glass was annealed at 770 °C for various durations.

The in-house XRD patterns of the samples prepared by annealing at 770 °C for various durations are shown in Fig. 2a. A broad halo pattern was observed in the data for the 0-h-annealed sample (pristine glass), indicating a completely disordered structure. Subtle diffraction peaks were observed at approximately 30° and 50° in the XRD patterns of the 2- and 3-h-annealed samples. Prominent diffraction peaks assigned to c- or t-$ZrO_2$ were found at approximately 30°, 35°, 50°, and 60° in the XRD patterns of the samples annealed longer than 4 h (shown as closed circles in Fig. 2a). The crystallite sizes of the samples

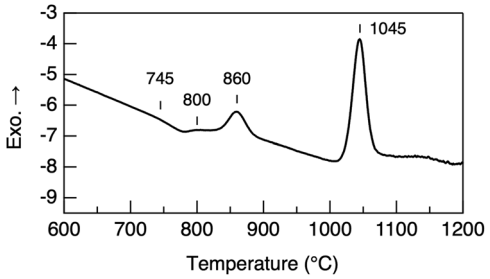


**Fig. 1** DSC curve at a heating rate of 10 °C $min^{-1}$ for Zr-doped lithium aluminosilicate glass.

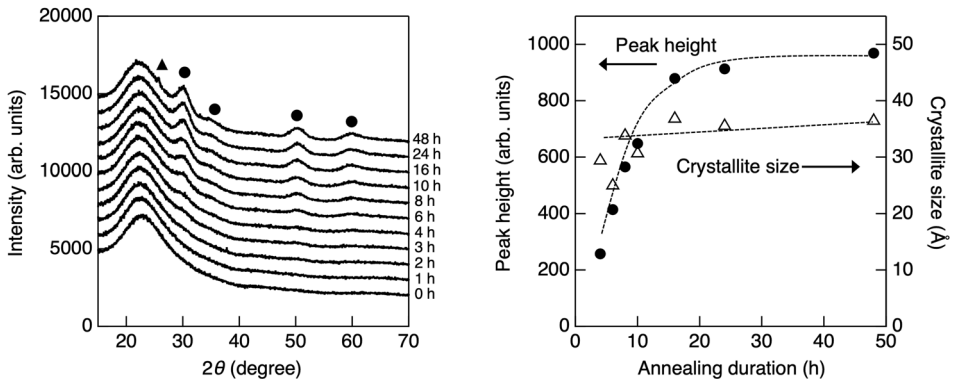


**Fig. 2 XRD data for the Zr-doped lithium aluminosilicate glass and glass-ceramics. a** In-house XRD patterns for the Zr-doped lithium aluminosilicate glass and glass-ceramics obtained by annealing at 770 °C for various annealing durations (shown on the right side of the figure). Closed circles and triangles: peak positions of cubic/tetragonal $ZrO_2$ and β-quartz solid solutions, respectively. **b** Annealing duration dependence of the peak height (closed circles) and crystallite size (open triangles) extracted from the diffraction peak observed at 30°.

annealed for longer than 4 h were calculated from the Scherrer equation using the peak width observed at 30°. The crystallite size and peak height versus annealing duration are shown in Fig. 2b. The annealing duration dependence of the crystallite size was considerably weaker than that of the peak height; thus, the thermal treatment increased the number of $ZrO_2$ crystallites rather than their size. Similar behavior was reported for the nuclei of $ZrO_2$[8] and $ZrTiO_4$[28] in $Li_2O$–$Al_2O_3$–$SiO_2$-based glasses. As shown in Fig. 2b, the generation of $ZrO_2$ crystallites was gradually saturated with successive annealing cycles. In the XRD pattern for the 48-h-annealed sample, an additional peak was observed at 26° (shown by the closed triangle in Fig. 2a) and was attributed to a peak of β-quartz s.s.[27]. The $ZrO_2$ crystallites gradually precipitated upon thermal treatment at 770 °C. Therefore, glass-ceramics suitable for investigating the structural changes during the initial nucleation stage were obtained.

### Analysis of nanoscale structure

The SAXS profiles of the samples prepared for various annealing durations are shown in Fig. 3a, b. A relatively low scattering intensity was observed for the 0-h-annealed sample, indicating that the pristine glass already had an internal inhomogeneous structure. The mean distance, $d$, between scatterers was calculated using $d = 2\pi/Q$, where $Q$ is the peak position in the SAXS profile. The calculated $d$ values and SAXS peak heights are shown in Fig. 3c. The SAXS peak height gradually increased with the annealing duration. These results indicated that the electron density contrast between the scatterers increased with increasing annealing duration. Conversely, the distance between scatterers was approximately 12 nm and did not show any notable change with increasing annealing duration, indicating that the spatial distribution of scatterers was unaffected by the thermal treatment.

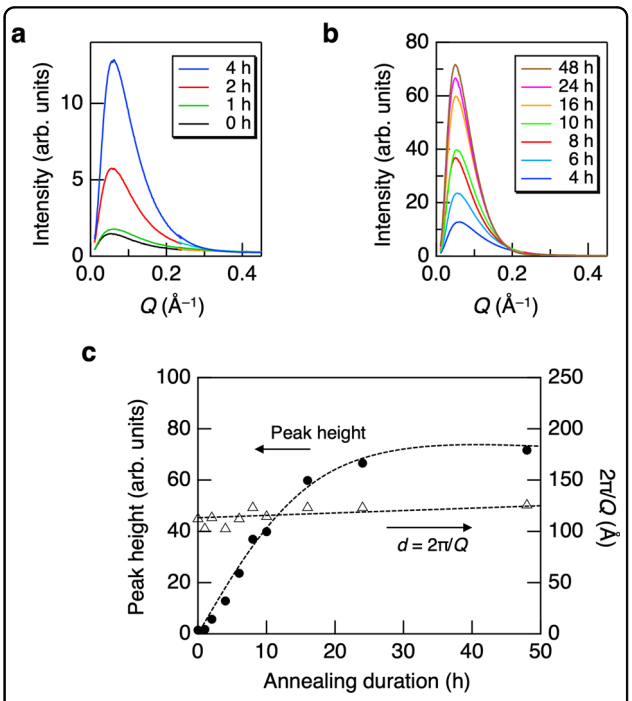


**Fig. 3 SAXS profiles and structural parameters for Zr-doped lithium aluminosilicate glass and glass-ceramics. a** SAXS profiles of the samples annealed for 0 h (black), 1 h (green), 2 h (red), and 4 h (blue). **b** SAXS profiles of the samples annealed for 4 h (blue), 6 h (cyan), 8 h (red), 10 h (green), 16 h (orange), 24 h (magenta), and 48 h (brown). **c**. Annealing duration dependence of the peak height (closed circles) and $2\pi/Q$ (open triangles) extracted from the SAXS profile.

As mentioned in the discussion of the XRD results, the size of the $ZrO_2$ crystallites was almost unchanged after

thermal treatment, whereas the number of $ZrO_2$ crystallites increased with annealing duration. If the SAXS profiles originated from the correlation between $ZrO_2$ crystallites, the SAXS peak position should shift to a higher $Q$ with the annealing duration because an increase in the number of $ZrO_2$ crystallites in a given volume could cause the particles to approach the others. Furthermore, explaining the generation of the peak in the SAXS profile of the pristine glass that does not include $ZrO_2$ crystallites is difficult. Therefore, correlations between the $ZrO_2$ crystallite particles are unlikely to account for the SAXS peaks in this system. Instead, the Zr-related phase separation was presumed to act as a scatterer for SAXS in this system. Based on the SAXS profile with a scattering peak for the 0-h-annealed sample, the internal phase separation into Zr-rich and Zr-poor phases in pristine glass was inherent. The thermal treatment at 770 °C induced the aggregation of $ZrO_x$ and subsequent partial precipitation of a $ZrO_2$ crystallite. Furthermore, with an increase in the annealing duration, the separation was enhanced without changing the distance between the scatterers. The internal phase separation in glasses was reported for $B_2O_3$–PbO–$Al_2O_3$[29] and $Al_2O_3$–$SiO_2$[30] glass systems. In these systems, the phase separations were characterized as binodal or spinodal[31] textures by Porod analysis of the SAXS patterns. In contrast, the SAXS profiles of pristine glass and glass-ceramics in this study showed a clear scattering peak and did not obey Porod's law, causing difficulty to characterize the phase separation behavior in the initial stage of nucleation based on the Porod plot. Based on the XRD patterns, the generation of a particularly large number of $ZrO_2$ crystallites was induced by thermal treatment. However, the SAXS data indicated that the separation between the Zr-rich and Zr-poor phases was inherent in pristine glass and increased with increasing annealing duration. The results from the combined in-house XRD and SAXS measurements indicated that the structural change in the Zr-containing lithium aluminosilicate glass-ceramic during the initial stage of nucleation originated from the separation between the Zr-rich and Zr-poor phases and that $ZrO_2$ crystallites precipitated in the Zr-rich phase. Notably, these structural changes occurred without any change in the spatial nanoscale geometry.

Nanoscale heterogeneities and the formation of nanocrystals have been reported in TEM-based studies of several $ZrO_2$-containing lithium aluminosilicate systems. Kleebusch et al. used a combination of XANES and TEM to report the formation of Zr-rich phase separation droplets, which evolved into crystalline $ZrO_2$ in $Li_2O$–$Al_2O_3$–$SiO_2$ glass-ceramics[8]. Höche et al. reported the precipitation of $ZrTiO_4$ nanocrystals in phase-separated droplets accompanied by the formation of a circumjacent shell consisting of an Al-rich region in $Li_2O$–$Al_2O_3$–$SiO_2$ glass-ceramics using TEM[32]. Raghuwanshi et al. quantitatively evaluated the core–shell structure using anomalous SAXS[33]. Based on these aforementioned studies, the growth of nanoprecipitates was constrained by a shell-like region[8,32,33]. The XRD results indicated that the size of the $ZrO_2$ crystallites was almost unchanged upon thermal treatment; thus, the $ZrO_2$ crystallites that precipitated in the Zr-rich phase potentially formed a core–shell-like structure, and in the shell region, the growth of nanoprecipitates was prevented.

### Analysis of the short-range Zr-centric structures by XAFS

To obtain clear insight into the structural changes in the short- and intermediate-range scales in the initial nucleation stage in the $ZrO_2$-containing glass-ceramic, we conducted structural analyses using a combination of XAFS and AXS measurements. These measurements were performed at the Zr K-edge to investigate Zr-specific structural information.

The Zr K-edge XANES spectra of the samples prepared for various annealing durations are shown in Fig. 4a. The edge jump position did not change between these spectra, indicating that the valence state of the Zr ion was tetravalent and was unchanged with the annealing duration. However, the shape of the XANES spectra gradually changed with annealing duration, indicating that the structure around the $Zr^{4+}$ ions gradually changed. Moreover, the isosbestic points (indicated by arrows in Fig. 4a) were observed in all XANES spectra; thus, the XANES spectra were formed by the superposition of the XANES spectra of the two states. These results were consistent with the aforementioned SAXS results, in which a structural change related to the separation between the Zr-rich and Zr-poor phases was proposed. The XANES spectrum of the 0-h-annealed sample (pristine glass) likely consisted of Zr-rich and Zr-poor phases without the precipitation of $ZrO_2$ crystallites. In contrast, a larger portion of the XANES spectrum of the 48-h-annealed sample should consist of the Zr-rich phase in which $ZrO_2$ crystallites were precipitated by thermal treatment. The XANES spectra of the 0- and 48-h-annealed samples were compared with those of the standard crystalline samples in Fig. 4b. In this study, we used YSZ, with a stable c-$ZrO_2$ at room temperature, and monoclinic (m-) $ZrO_2$ as the standard crystalline materials. A comparison of these XANES spectra indicated that the structure of the sample changed from a glass-like disordered structure to a crystal-like ordered structure because the XANES spectra of standard crystalline materials were more similar to those of the 48-h-annealed sample than to those of the 0-h-annealed sample. Moreover, in the XANES spectrum of the 48-h-annealed sample, the multiple scattering feature[34] observed in the XANES spectra of t-$ZrO_2$ and YSZ[35] was observed as a small rounded peak at approximately 18030 eV (indicated

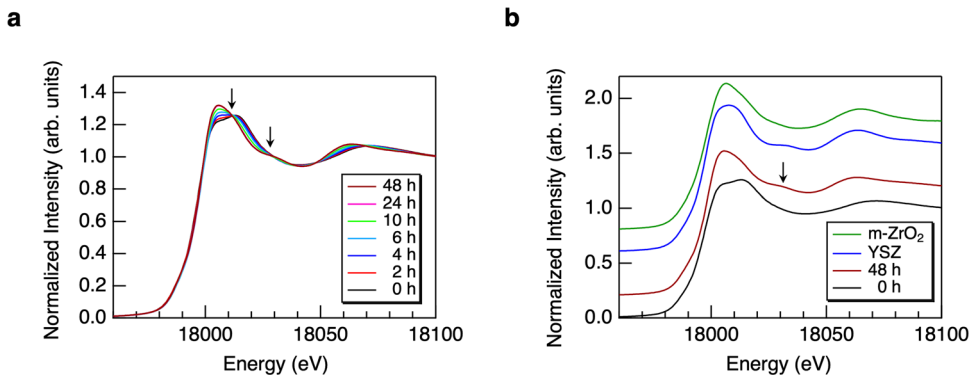


**Fig. 4 XANES spectra of Zr-doped lithium aluminosilicate glass/glass-ceramics and $ZrO_2$ crystals. a** XANES spectra of samples annealed for 0 h (black), 2 h (red), 4 h (blue), 6 h (cyan), 10 h (green), 24 h (magenta), and 48 h (brown). The arrows mark the isosbestic points. **b** XANES spectra of samples annealed for 0 h (black) and 48 h (brown) along with those of YSZ (blue) and monoclinic zirconia (m-$ZrO_2$) (green). The arrow indicates multiple scattering, which is a characteristic feature of tetragonal $ZrO_2$[34] and cubic $ZrO_2$ in YSZ[35].

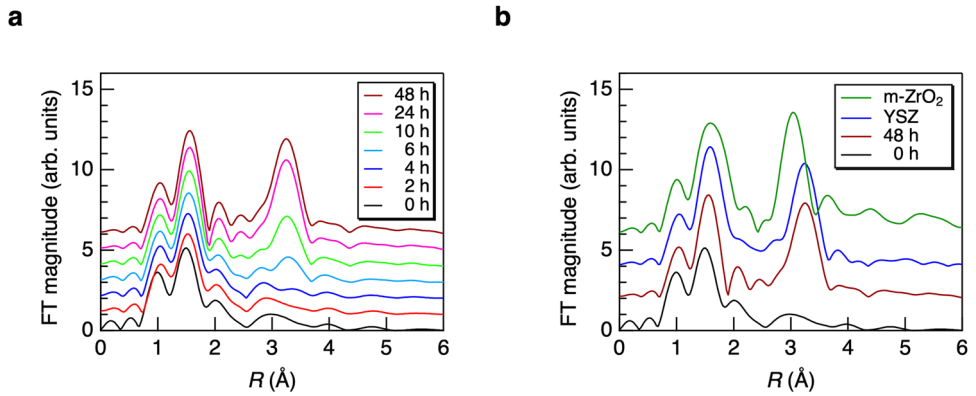


**Fig. 5 Fourier transform of $k^3$-weighted EXAFS functions for Zr-doped lithium aluminosilicate glass/glass-ceramics and $ZrO_2$ crystals. a** Fourier transform of the $k^3$-weighted EXAFS functions of the samples annealed for 0 h (black), 2 h (red), and 4 h (blue), 6 h (cyan), 10 h (green), 24 h (magenta), and 48 h (brown). **b** Fourier transform of the $k^3$-weighted EXAFS functions of the samples annealed for 0 h (black) and 48 h (brown) along with those for YSZ (blue) and monoclinic zirconia (m-$ZrO_2$) (green).

by the arrow in Fig. 4b). Based on these results for the 48-h-annealed sample, either a Zr-related local structural order formed in the c-$ZrO_2$ (YSZ) or t-$ZrO_2$ was introduced into its structure.

The FT $k^3$-weighted EXAFS spectra of the samples are shown in Fig. 5a. The first peak in the FT spectra observed at approximately 1.6 Å was assigned to the Zr–O nearest-neighbor correlation. The distance observed in the FT $k^3$-weighted EXAFS spectra shown in Fig. 5a, b was approximately 0.2–0.5 Å shorter than the actual distance because of the phase shift[9]. The Zr–O distance slightly shifted to a longer $R$ with the annealing duration. The second nearest-neighbor peak appeared at approximately 3.0–3.2 Å for the samples annealed for 6 h or more; the peak became stronger with increasing annealing duration. The Zr–O distances and coordination numbers in the 0-, 2-, 4-, 6-, 10-, 24-, and 48-h-annealed samples were determined by curve fitting to their EXAFS spectra; these findings are summarized in Table 2. The Zr–O coordination number gradually increased over 4 h of annealing and reached approximately 7 after 48 h. An increase in the Zr–O coordination number associated with nucleation was reported in previous XAFS studies of lithium aluminosilicate systems[5,6,8]. Similarly, an increase in the Ti–O coordination number during nucleation was reported in lithium aluminosilicate glass that contained $TiO_2$ as a nucleation agent in XANES studies[36]. Thus, an increase in the coordination number around a cation in the nucleation agent was a general trend during the nucleation of the aluminosilicate glasses. The FT $k^3$-weighted EXAFS spectra of the 0- and 48-h-annealed samples are shown along with those of the standard YSZ and m-$ZrO_2$ samples in Fig. 5b. The first and second peak positions were almost the same for the 48-h-annealed and YSZ samples

**Table 2 Coordination number and distance of Zr–O obtained by EXAFS analysis. The Debye–Waller factors were fixed to 0.009 Å$^2$ in all curve fittings.**

| Samples | 0 h | 2 h | 4 h | 6 h | 10 h | 24 h | 48 h |
|---|---|---|---|---|---|---|---|
| $r_{Zr-O}$ (Å) | 2.03 ± 0.04 | 2.05 ± 0.03 | 2.06 ± 0.04 | 2.07 ± 0.04 | 2.07 ± 0.05 | 2.07 ± 0.04 | 2.06 ± 0.03 |
| $N_{Zr-O}$ | 5.3 ± 1.7 | 5.2 ± 1.7 | 5.5 ± 1.7 | 5.9 ± 1.7 | 6.2 ± 1.6 | 6.5 ± 1.5 | 6.9 ± 1.9 |

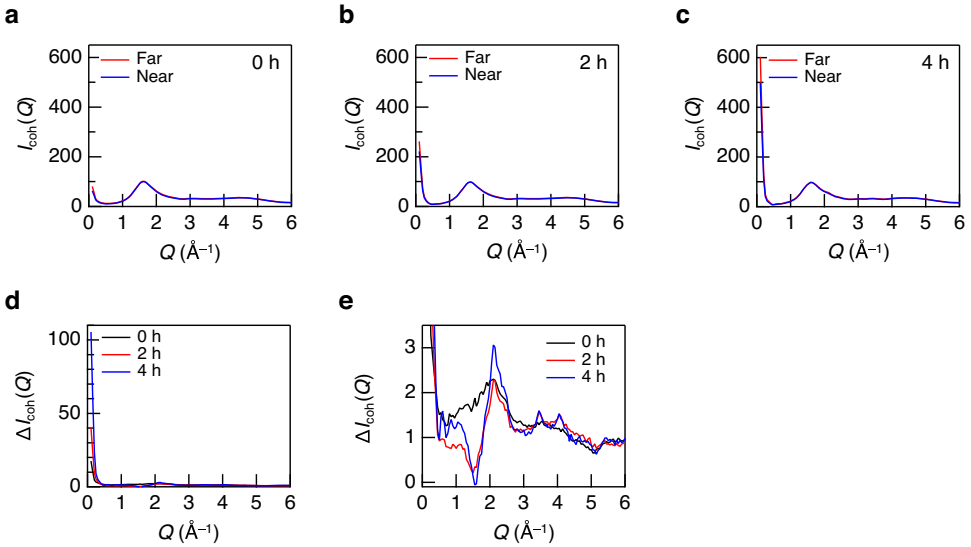


**Fig. 6 X-ray scattering intensities and differential intensities for Zr-doped lithium aluminosilicate glass/glass-ceramics. a** X-ray scattering intensities measured at $E_{far}$ (red) and $E_{near}$ (blue) for the 0-h-annealed sample. **b** X-ray scattering intensities measured at $E_{far}$ (red) and $E_{near}$ (blue) for the 2-h-annealed sample. **c** X-ray scattering intensities measured at $E_{far}$ (red) and $E_{near}$ (blue) for the 4-h-annealed sample. **d** Differential intensities between two X-ray scattering intensities measured at $E_{far}$ and $E_{near}$ for the samples annealed for 0 h (black), 2 h (red), and 4 h (blue). **e** Enlarged view of the high-$Q$ region of the differential intensities of the samples annealed for 0 h (black), 2 h (red), and 4 h (blue).

but differed greatly between the 48-h-annealed and m-$ZrO_2$ samples; these results indicated that the $ZrO_2$ microcrystalline phase generated by thermal treatment was not monoclinic. The slight difference between the FT $k^3$-weighted EXAFS spectra of the 48-h-annealed and YSZ samples indicated the presence of residual $Zr^{4+}$ ions in the glassy phase in the 48-h-annealed sample or the structural distortion around $Zr^{4+}$ ions in the 48-h-annealed and/or YSZ sample. The structural changes in the post-nucleation stage were elucidated by Zr–O coordination number analyses using EXAFS data. However, the second nearest-neighbor correlation, which provides crucial information in the early stage of nucleation, was barely observed in the FT $k^3$-weighted EXAFS spectra of the pristine glass and 2–4-h-annealed samples. Thus, the local structure around the $Zr^{4+}$ ions for the pristine glass and the 2–4-h-annealed glass-ceramic samples was considerably disordered for the observation of the second nearest-neighbor correlations performed with the EXAFS measurements. Thus, in principle, observing atomic correlations beyond the first coordination shell in our samples during the early stage of nucleation using EXAFS was difficult. Thus, we analyzed the AXS data to determine a Zr-specific structure beyond the nearest-neighbor correlations.

### Analysis of the Zr-related structures at short- and intermediate-range scales by AXS

Figure 6a–c show the X-ray scattering intensities $I_{coh}(Q)$ measured at $E_{far}$ and $E_{near}$ after annealing the samples for 0, 2, and 4 h. The $I_{coh}(Q)$ measured at $E_{far}$ was slightly greater than that measured at $E_{near}$. The first sharp diffraction peak (FSDP) was observed at approximately 1.6 Å$^{-1}$, which was close to the position of the FSDP of $SiO_2$ glass[37], in all X-ray scattering patterns shown in Fig. 6a–c. Because more than 70% of the components of the sample are $SiO_2$, the FSDP was mainly attributed to a network structure stemming from the $SiO_2$ glass, which consisted of $SiO_4$ tetrahedra with shared oxygen atoms at the corners. The differences in the positions and shapes of the FSDPs among the 0-, 2-, and 4-h-annealed samples were minimal, indicating that the $SiO_4$ tetrahedral

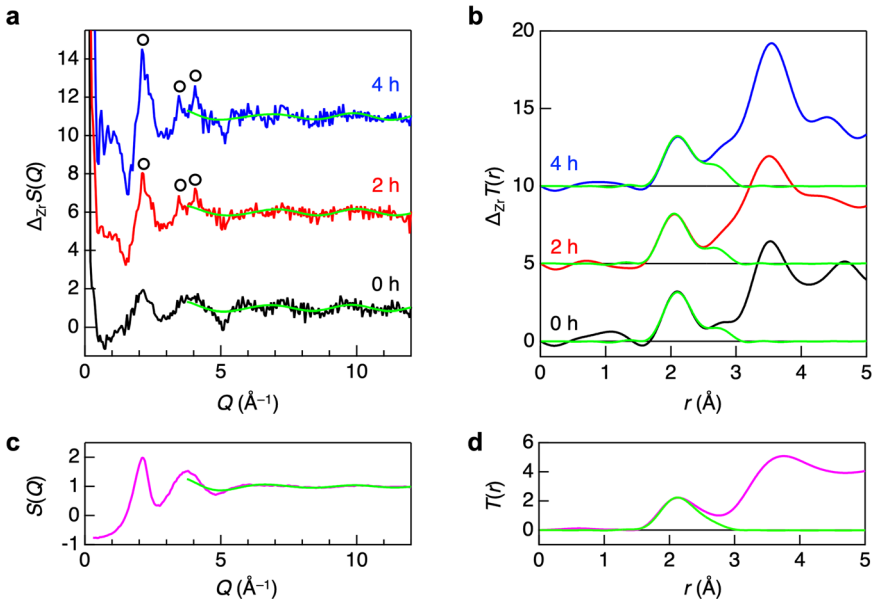


**Fig. 7 Differential and total structure factors and differential and total correlation functions for Zr-doped lithium aluminosilicate glass/glass-ceramics and liquid $ZrO_2$.** **a** Differential structure factor $\Delta_{Zr}S(Q)$ and **b** differential total correlation function $\Delta_{Zr}T(r)$ of the samples annealed for 0 h (black), 2 h (red), and 4 h (blue). **c** X-ray total structure factor $S(Q)$ and (**d**) X-ray total correlation functions $T(r)$ for liquid $ZrO_2$ at 2800 °C[38]. The $S(Q)$ and $T(r)$ values calculated using the pair function method are plotted as green curves.

network did not change significantly upon thermal treatment. The $I_{coh}(Q)$ values measured at both $E_{far}$ and $E_{near}$ increased at $Q < 0.5$ Å$^{-1}$ with increasing annealing duration. The increasing scattering intensity at $Q < 0.5$ Å$^{-1}$ was potentially due to the inhomogeneity at the nanoscale caused by thermal treatment, as mentioned in the discussion of the SAXS results. In addition, the differential intensity $\Delta I_{coh}(Q)$ between the two scattering intensities measured at $E_{far}$ and $E_{near}$, as shown in Fig. 6d, increased at $Q < 0.5$ Å$^{-1}$ with increasing annealing duration; thus, the phase separation enhancement by thermal treatment was related to $Zr^{4+}$. The behavior of $\Delta I_{coh}(Q)$ in the lower-$Q$ region supported the SAXS results. Furthermore, $\Delta I_{coh}(Q)$ significantly changed in the higher-$Q$ region ($Q > 0.5$ Å$^{-1}$), as shown in Fig. 6e, indicating that the Zr-related structure at short- and intermediate-range scales underwent changes upon thermal treatment.

Figure 7a shows the differential structure factors $\Delta_{Zr}S(Q)$ for the 0-, 2-, and 4-h-annealed samples. The first peak of $\Delta_{Zr}S(Q)$ for the 0-h-annealed sample was observed at approximately 2.1 Å$^{-1}$; this was different from the position of the FSDP observed in the X-ray scattering intensities. Therefore, the scale of the periodicity related to $Zr^{4+}$ was different from that related to the $SiO_4$ network. The total structure factor, $S(Q)$, for liquid $ZrO_2$[38] is shown in Fig. 7c. The positions of the first peak of $\Delta_{Zr}S(Q)$ for the 0-h-annealed sample and $S(Q)$ for liquid $ZrO_2$ were significantly close, indicating that the periodicity related to $Zr^{4+}$ in pristine glass was similar to that in liquid $ZrO_2$. Compared with that of pristine glass, the first peak positions of $\Delta_{Zr}S(Q)$ for the 2- and 4-h-annealed samples did not shift but became sharper with an increase in the annealing duration. In addition, the minute Bragg peaks (shown as open circles in Fig. 7a) appeared in $\Delta_{Zr}S(Q)$ for the 2- and 4-h-annealed samples. The peak positions were close to the diffraction peaks of c- or t-$ZrO_2$, indicating that the initial crystal nucleus was formed during the annealing of pristine glass in a short time. Furthermore, compared to in-house XRD measurements, AXS measurements enable more sensitive detection of crystallization behavior involving a specific element.

Differential total correlation functions, $\Delta_{Zr}T(r)$, for the 0-, 2-, and 4-h-annealed samples and the total correlation function, $T(r)$, for liquid $ZrO_2$ obtained from the Fourier transforms of $\Delta_{Zr}S(Q)$ and $S(Q)$ are shown in Fig. 7b, d, respectively. The Zr–O correlation peak was located at 2.1 Å for all $\Delta_{Zr}T(r)$ and $T(r)$ values. For liquid $ZrO_2$, the asymmetric Zr–O correlation peak with a tail of approximately 2.8 Å indicated the formation of distorted $ZrO_x$ polyhedra[38]. The second peak, with a shoulder on the low-$r$ side, was observed at 3.6 Å for all $\Delta_{Zr}T(r)$ values. In the case of liquid $ZrO_2$, the second peak observed at 3.6 Å in $T(r)$ was assigned to the Zr–Zr correlation, corresponding to the distance between the centers of $ZrO_x$ polyhedra with a large fraction of edge sharing of oxygen in addition to corner sharing[38]. In the crystalline materials, a Zr–Zr distance of approximately 3.6 Å

corresponding to the edge sharing of $ZrO_8$ polyhedra was observed for t-$ZrO_2$ and crystalline $ZrSiO_4$ (zircon)[39]. Thus, the second peak in $\Delta_{Zr}T(r)$ was assigned mainly to the Zr–Zr correlation corresponding to edge- and corner-sharing of $ZrO_x$ polyhedra. The Zr–Si, Zr–Al, and second-neighbor Zr–O correlations contributed to the second peak in $\Delta_{Zr}T(r)$ in addition to the Zr–Zr correlations according to Eq. (6). The shoulder peak on the low-$r$ side of the second peak was likely composed of the tail of the asymmetric Zr–O peak and other Zr-related correlation peaks; this peak was observed at approximately 2.8–2.9 Å for all $\Delta_{Zr}T(r)$ values. In Eq. (6), only six partials contribute to $\Delta_{Zr}S(Q)$, and the weighting factors for Zr–Si and Zr–Al correlations are relatively large, with the exception of the Zr–O correlation in $\Delta_{Zr}S(Q)$; therefore, we could estimate that the shoulder peak mainly consisted of the Zr–Si and/or the Zr–Al correlation superposed on the tail of the Zr–O peak. Both the second and shoulder peaks of $\Delta_{Zr}T(r)$ evolved with increasing annealing duration, indicating that the development of Zr-related structural ordering beyond the nearest-neighbor distance was induced by thermal treatment.

The Zr–O coordination numbers of the 0-, 2-, and 4-h-annealed samples and liquid $ZrO_2$ were determined using the pair function method proposed by Mozzi and Warren[40]. The pair function is a useful method for analyzing real-space functions, from which the structural parameters such as the interatomic distance and coordination number can be estimated. From the concept of the pair function, the calculated total correlation function $T^{calc}(r)$ was obtained using the following equation for the distance $r_{Zr-O}$ and coordination number $N_{Zr-O}$ of the Zr–O pair:

$$T^{calc}_{Zr\text{-}O}(r) = \frac{2}{\pi}\int_{Q_{min}}^{Q_{max}} \frac{2c_{Zr}N_{Zr\text{-}O}f_{Zr}(Q)f_O(Q)}{\langle f(Q)\rangle^2}\exp\left(-\frac{1}{2}l^2_{Zr\text{-}O}Q^2\right)\frac{\sin(\pi Q/Q_{max})}{\pi Q/Q_{max}}\frac{\sin(Qr_{Zr\text{-}O})}{r_{Zr\text{-}O}}\sin Qr\,dQ. \quad (7)$$

The term $l_{Zr\text{-}O}$ is a convergence factor that represents the static and thermal disorders of the Zr–O correlation. In contrast, the calculated differential total correlation function $\Delta T^{calc}(r)$ was obtained using the following equation:

$$\Delta T^{calc}_{Zr\text{-}O}(r) = \frac{2}{\pi}\int_{Q_{min}}^{Q_{max}} \frac{2c_{Zr}N_{Zr\text{-}O}\Delta_{Zr}[f_{Zr}(Q)f_O(Q)]}{\Delta_{Zr}\left[\langle f(Q)\rangle^2\right]}\exp\left(-\frac{1}{2}l^2_{Zr\text{-}O}Q^2\right)\frac{\sin(\pi Q/Q_{max})}{\pi Q/Q_{max}}\frac{\sin(Qr_{Zr\text{-}O})}{r_{Zr\text{-}O}}\sin Qr\,dQ. \quad (8)$$

The Zr–O coordination numbers can be estimated by fitting the calculated $\Delta T(r)$ and $T(r)$ for the Zr–O correlation to the experimental $\Delta_{Zr}T(r)$ and $T(r)$. We adopted two Zr–O pair functions to reproduce the asymmetric Zr–O peak in $\Delta_{Zr}T(r)$ and $T(r)$. In this procedure, the variations in the $r_{Zr-O}$ and $N_{Zr-O}$ in the calculated $\Delta T(r)$ and $T(r)$ were ±0.02 Å and ±0.3, respectively. The $\Delta_{Zr}S(Q)$, $S(Q)$, $\Delta_{Zr}T(r)$, and $T(r)$, along with the results from the pair function method (green curve), are shown in Fig. 7a–d, respectively. As shown in Fig. 7a, c, good agreement between the pair function and the experimental data was obtained at $Q > 3.8$ Å$^{-1}$. The structural parameters obtained using the pair-function method are summarized in Table 3. In the case of liquid $ZrO_2$, both the distance and average coordination number of Zr–O were in agreement with those obtained by the density functional–molecular dynamics simulation reported by Kohara et al.[38]. The Zr–O coordination number for the annealed samples increased from 5.1 to 6.0 with increasing annealing duration. This increase in the Zr–O coordination number for the 0-, 2-, and 4-h-annealed samples was not observed from the EXAFS analysis, as shown in Table 2, because the presence of an asymmetric atomic distribution reduced the amplitude of the EXAFS signal; this reduction in amplitude is frequently accompanied by reductions in the bond distance and coordination number. In contrast, the analysis of AXS data using the pair function method enabled the use of two Zr–O pair functions to reproduce the asymmetric Zr–O peak in $\Delta_{Zr}T(r)$ and $T(r)$. These total correlation functions quantitatively described the atomic pair distribution in glassy materials, enabling the direct analysis of the asymmetric atomic correlation peaks. A successive increase in the Zr–O coordination number from 5.1 to 6.0 was achieved during nucleation in a glass structure because the rigid glass network sustained a metastable structural unit of the $Zr^{4+}$ ion in the glass matrix. The Zr–O coordination number of 6.0 for the 4-h-annealed sample was similar to that of liquid $ZrO_2$, indicating that a liquid-like local structural motif around a $Zr^{4+}$ ion was formed during the initial nucleation stage.

The Zr–Si and/or Zr–Al correlations observed as the shoulder peak in $\Delta_{Zr}T(r)$ corresponded to the distance between the centers of the $ZrO_x$ polyhedra and the (Si/Al)$O_4$ tetrahedra. The Zr–(Si/Al) distance of 2.8–2.9 Å was considerably short for the Si or Al at the center of a (Si/Al)$O_4$ tetrahedron sharing an oxygen at the corner with a $ZrO_x$ polyhedron. Therefore, the short Zr–(Si/Al) distance indicated the formation of edge-sharing polyhedral connections between $ZrO_x$ and (Si/Al)$O_4$. A short Zr–Si distance of 2.98 Å corresponding to edge sharing between $ZrO_8$ and $SiO_4$ was observed in zircon[39]. Furthermore, using EXAFS analyses, Cormier et al. determined that the Zr–(Si/Al) distance at approximately 3.1 Å corresponded to edge sharing between $ZrO_6$ or $ZrO_7$ and (Si/Al)$O_4$ in Zr-containing aluminosilicate glasses[7]. The presence of

**Table 3 Structural parameters derived by the pair function method.**

| Samples | 0 h | | 2 h | | 4 h | | Liquid $ZrO_2$ | |
|---|---|---|---|---|---|---|---|---|
| | Zr–O(1) | Zr–O(2) | Zr–O(1) | Zr–O(2) | Zr–O(1) | Zr–O(2) | Zr–O(1) | Zr–O(2) |
| $r_{Zr-O}$ (Å) | 2.10 ± 0.02 | 2.67 ± 0.02 | 2.05 ± 0.02 | 2.63 ± 0.02 | 2.10 ± 0.02 | 2.63 ± 0.02 | 2.09 ± 0.02 | 2.49 ± 0.02 |
| $l_{Zr-O}$ (Å$^2$) | 0.01 | 0.01 | 0.01 | 0.01 | 0.01 | 0.01 | 0.09 | 0.09 |
| $N_{Zr-O}$ | 3.8 ± 0.3 | 1.3 ± 0.3 | 3.8 ± 0.3 | 1.3 ± 0.3 | 3.9 ± 0.3 | 2.1 ± 0.3 | 4.0 ± 0.3 | 1.7 ± 0.3 |
| Total $N_{Zr-O}$ | 5.1 | | 5.3 | | 6.0 | | 5.7 | |

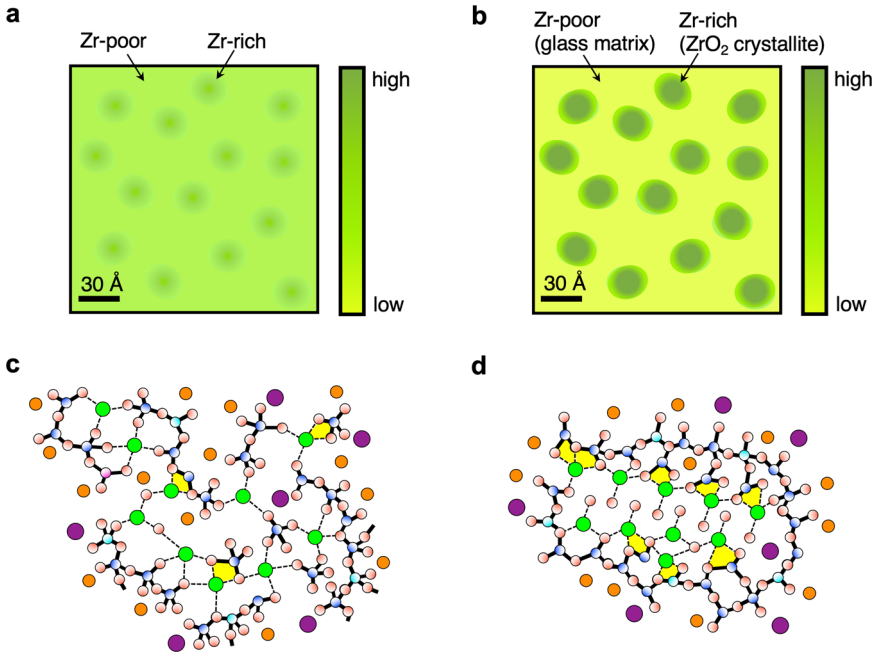


**Fig. 8 Schematic representation of the initial nucleation stage in zirconium-doped aluminosilicate glass and glass-ceramics.** Nanoscale structures of the 0-h-annealed sample (pristine glass) (**a**) and 4-h-annealed sample (**b**). Representations of the intermediate-range structure in the Zr-rich phase for pristine glass (**c**) and the 4-h-annealed sample (**d**). Green: zirconium, blue: silicon, cyan: aluminum, magenta: phosphorus, orange: lithium, purple: sodium, and red: oxygen. The yellow polyhedra indicate edge-sharing polyhedral connections.

the shoulder peak in $\Delta_{Zr}T(r)$ for the 0-h-annealed sample indicated the inherent edge-sharing polyhedral connection in pristine glass; this was not a typical structural feature of glass-forming materials. The shoulder peak in $\Delta_{Zr}T(r)$ increased with annealing duration, indicating that thermal treatment promoted the formation of edge-sharing structures. Thus, we determined that a liquid-like local structural motif around a $Zr^{4+}$ ion and the edge-sharing structures between $ZrO_x$ polyhedra and $(Si/Al)O_4$ tetrahedra were formed by thermal treatment of the pristine glass. These Zr-related structural changes likely played a key role in the initial stages of nucleation.

To obtain clear insights into the initial stage of nucleation from the atomic scale to the nanoscale, we constructed a schematic representation of the structural change from the pristine glass to glass-ceramic after 4 h of annealing, as shown in Fig. 8a–d. Figure 8a, b show a comparison of the representations of the nanoscale structures based on the XRD and SAXS results for the pristine glass and the 4-h-annealed sample, respectively. As shown by the SAXS results, pristine glass had an inherent phase separation between the Zr-rich and Zr-poor regions (Fig. 8a). The electron density in the Zr-rich region was greater than that in the Zr-poor region. Thermal treatment of the pristine glass for 4 h caused aggregation of $ZrO_x$ and an increase in contrast in the electron density between the Zr-rich and Zr-poor phases (Fig. 8b). The precipitation of $ZrO_2$ crystallites in the Zr-rich regions occurred only during the 2–4-h

annealing of pristine glass (Fig. 7a). Moreover, the crystallite size of approximately 30 Å did not increase with the annealing duration, whereas the number of $ZrO_2$ crystallites increased. Similar phase separation behavior during the nucleation process, in which the growth of nanoprecipitates was limited by the size of the phase-separated domains, was reported for various glass-ceramics[8,28,32,33]. In these cases, nanoscale heterogeneities, consisting of precipitated nanocrystals and a glass matrix, played an important role in yielding glass-ceramics that exhibited excellent mechanical and thermal properties while maintaining their transparency[1,2]. The addition of small amounts of nucleation agents to the host glass induced phase separation at the nanoscale[3,32,41]. DeCeanne et al. proposed the following definition of a nucleation agent: "a nucleating (nucleation) agent is a minority component of the glass composition that leads to increased internal nucleation rates or precipitation and control of desired crystal phases, either by lowering the thermodynamic or the kinetic barrier for nucleation, or some combination thereof"[3]. Thus, phase separations induced by nucleation agents could affect the thermodynamics or kinetics of nucleation by forming functional phases (e.g., the Zr-rich regions shown in Fig. 8b) that could act as precursors to nanocrystals, leading to enhanced nucleation. Figure 8c, d show schematic representations of the intermediate-range structure in the Zr-rich region for pristine glass and the 4-h-annealed sample, respectively. In the pristine glass, $SiO_4$, $AlO_4$, and only a few $PO_4$ polyhedra formed a tetrahedral network, whereas $Zr^{4+}$, $Li^+$, and $Na^+$ cations were distributed around the network (Fig. 8c). Several $Zr^{4+}$ ions formed an edge-sharing structure with the $(Si/Al)O_4$ tetrahedra in the structure of pristine glass. After annealing for 4 h, the structure became more ordered and was centered on a Zr cluster, as shown in Fig. 8d. Compared to the structure of pristine glass, $Zr^{4+}$ ions congregated and formed an ordered arrangement, whereby the Zr–O coordination number increased and additional edge-sharing structures formed between $ZrO_x$ and surrounding $(Si/Al)O_4$ tetrahedra. This specific configuration involving $Zr^{4+}$ ions could be the initial crystal nucleus of the Zr-doped lithium aluminosilicate glass-ceramic. The Zr-related configuration formed a periodic c- or t-$ZrO_2$-like structure ($ZrO_2$ nanocrystal) during annealing for 2–4 h, generating the Bragg peaks in the differential structure factor $\Delta_{Zr}S(Q)$ (Fig. 7a). This finding was consistent with the SAXS results because the difference in the electron density between the congregated $Zr^{4+}$ ions (Zr-rich phase) and the other ions (Zr-poor phase) increased with the formation of an ordered arrangement of $Zr^{4+}$ ions in the Zr-rich phase. The $ZrO_2$ nanocrystal surrounded by the $(Si/Al)O_4$ tetrahedral network shown in Fig. 8d corresponded to the core–shell structure reported in previous studies[8,32,33,36], as mentioned in the discussion of the SAXS results. The shell structure, consisting of a $(Si/Al)O_4$ tetrahedral network, could act as a nucleation barrier that prohibited the growth of $ZrO_2$ crystals. This behavior supported the theoretical model predicted by the generalized Gibbs approach[42]; here, the composition and structure of a nucleus significantly changed, while the size remained nearly constant in the early stage of nucleation. Hence, our proposed model for the initial crystal nucleus of $ZrO_2$ (Fig. 8d) was consistent with both nanoscale structural studies[8,32,33,36] and the theoretical approach[42]. Notably, the short Zr–(Si/Al) correlations, described as Zr–O–(Si/Al) bonds in Fig. 8c, d, played important roles in the formation of the initial crystal nucleus. Zr–(Si/Al) correlations beyond the nearest-neighbor distance have been rarely observed using conventional approaches; however, we succeeded in their investigation by using Zr-specific PDF analysis with AXS data. These findings may provide new insights into the intermediate-range structure of nucleation agents in glasses and promote a better understanding of the nucleation mechanism in the initial stages of glass-ceramic materials.

In this study, we performed a state-of-the-art multiscale structural analysis by combining XRD, SAXS, XAFS, and AXS measurements. Based on a comprehensive analysis of the atomic-to-nanoscale structure, we succeeded in the determination of the Zr-related intermediate-range structure that was the initial crystal nucleus for the nucleation process in lithium aluminosilicate glass. Multiscale structural analysis combined with the element-specific measurements enabled the attainment of crucial information to elucidate the relationship between the structures and material properties in multicomponent disordered systems.

#### Acknowledgements

This work was partially supported by JSPS Grant-in-Aid for Transformative Research Areas (A) "Hyper-Ordered Structures Science" (grant numbers 20H05878 (to S.K.), 20H05881 (to Y.O., H.T. and S.K.)), and for Scientific Research (C) (grant number 19K05648 (to Y.O.)). Synchrotron radiation experiments were performed at BL13XU of SPring-8 with the approval of the Japan Synchrotron Radiation Research Institute (JASRI) (Proposal No. 2019A1722) and at BL5S1 and BL8S3 of the Aichi Synchrotron Radiation Center (Approval Nos. 2019D1001 and 2019D1002).

#### Author details

[1]Center for Basic Research on Materials, National Institute for Materials Science, 1-2-1 Sengen, Tsukuba, Ibaraki 305-0047, Japan. [2]Institute for Integrated Radiation and Nuclear Science, Kyoto University, 2-1010 Asashiro-nishi, Kumatori-cho, Sennan-gun, Osaka 590-0494, Japan. [3]Innovative Technology Laboratories, AGC, Inc., 1-1 Suehiro-cho, Tsurumi-ku, Yokohama, Kanagawa 230-0045, Japan. [4]Materials Integration Laboratories, AGC, Inc., 1-1 Suehiro-cho, Tsurumi-ku, Yokohama, Kanagawa 230-0045, Japan. [5]Scattering and Imaging Division, Japan Synchrotron Radiation Research Institute (JASRI, SPring-8), 1-1-1 Kouto, Sayo-gun, Hyogo 679-5198, Japan. [6]Spectroscopy Division, Japan Synchrotron Radiation Research Institute (JASRI, SPring-8), 1-1-1 Kouto, Sayo-cho, Sayo-gun, Hyogo 679-5198, Japan

#### Author contributions

Y.O. and Y.T. designed the study. The samples were prepared by H.H. and Q.L. Differential scanning calorimetry was performed by H.H. Small-angle X-ray scattering was conducted by Y.T. X-ray absorption was performed by Y.T. and T.I. Anomalous X-ray scattering was conducted by Y.O., Y.T., H.T. and S.K. The obtained data were analyzed by Y.O., Y.T., H.H., T.I. and S.K. The manuscript was written by Y.O., Y.T. and S.K. with input from all authors.

**Conflict of interest**
The authors declare no competing interests.

**Publisher's note**
Springer Nature remains neutral with regard to jurisdictional claims in published maps and institutional affiliations.

**Supplementary information** The online version contains supplementary material available at https://doi.org/10.1038/s41427-024-00542-y.

Received: 9 August 2023 Revised: 31 January 2024 Accepted: 18 March 2024.
Published online: 19 April 2024

**References**

1. Beall, G. H. & Pinckney, L. R. Nanophase glass-ceramics. *J. Am. Ceram. Soc.* **82**, 5–16 (1999).
2. Zanotto, E. D. A bright future for glass-ceramics. *Am. Ceram. Soc. Bull.* **89**, 19–27 (2010).
3. DeCeanne, A. V., Rodrigues, L. R., Wilkinson, C. J., Mauro, J. C. & Zanotto, E. D. Examining the role of nucleating agents within glass-ceramic systems. *J. Non-Cryst. Solids* **591**, 121714 (2022).
4. Dargaud, O., Cormier, L., Menguy, N., Galoisy, L., Calas, G. & Papin, S. et al. Structural role of $Zr^{4+}$ as a nucleating agent in a MgO–$Al_2O_3$–$SiO_2$ glass-ceramics: a combined XAS and HRTEM approach. *J. Non-Cryst. Solids* **356**, 2928–2934 (2010).
5. Patzig, C., Höche, T., Hu, Y., Ikeno, H., Krause, M. & Dittmer, M. et al. Zr coordination change during crystallization of MgO–$Al_2O_3$–$SiO_2$–$ZrO_2$ glass ceramics. *J. Non-Cryst. Solids* **384**, 47–54 (2014).
6. Seidel, S., Patzig, C., Höche, T., Krause, M., Ebert, M. & Hu, Y. et al. The crystallization of MgO–$Al_2O_3$–$SiO_2$–$ZrO_2$ glass-ceramics with and without the addition of $Y_2O_3$ – a combined STEM/XANES study. *RSC Adv.* **6**, 62934 (2016).
7. Cormier, L., Dargaud, O., Calas, G., Jousseaume, C., Papin, S. & Trcera, N. et al. Zr environment and nucleation role in aluminosilicate glasses. *Mater. Chem. Phys.* **152**, 41–47 (2015).
8. Kleebusch, E., Patzig, C., Krause, M., Hu, Y., Höche, T. & Rüssel, C. The formation of nanocrystalline $ZrO_2$ nuclei in a $Li_2O$–$Al_2O_3$–$SiO_2$ glass – a combined XANES and TEM study. *Sci. Rep.* **7**, 10869 (2017).
9. Penner-Hahn, J. E. X-ray absorption spectroscopy in coordination chemistry. *Coord. Chem. Rev.* **190–192**, 1101–1123 (1999).
10. Fischer, H. E., Barnes, H. E. & Salmon, P. S. Neutron and X-ray diffraction studies of liquid and glasses. *Rep. Prog. Phys.* **69**, 233–299 (2006).
11. Kohara, S. & Salmon, P. S. Recent advances in identifying the structure of liquid and glassy oxide and chalcogenide materials under extreme conditions: a joint approach using diffraction and atomistic simulation. *Adv. Phys. X* **1**, 640–660 (2016).
12. Kohara, S. Atomistic and electronic structures of functional disordered materials revealed by a combination of quantum-beam measurements and computer simulations. *J. Ceram. Soc. Jpn.* **125**, 799–807 (2017).
13. Kohara, S., Suzuya, K., Takeuchi, K., Loong, C.-K., Grimsditch, M. & Weber, J. K. R. et al. Glass formation at the limit of insufficient network formers. *Science* **303**, 1649–1652 (2004).
14. Akola, J., Kohara, S., Ohara, K., Fujiwara, A., Watanabe, Y. & Masuno, A. et al. Network topology for the formation of solvated electrons in binary CaO–$Al_2O_3$ composition glasses. *Proc. Natl. Acad. Sci. USA* **110**, 10129–10134 (2013).
15. Onodera, Y., Kohara, S., Masai, H., Koreeda, A., Okumura, S. & Ohkubo, T. Formation of metallic cation–oxygen network for anomalous thermal expansion coefficients in binary phosphate glass. *Nat. Commun.* **8**, 15449 (2017).
16. Onodera, Y., Takimoto, Y., Hijiya, H., Taniguchi, T., Urata, S. & Inaba, S. et al. Origin of the mixed alkali effect in silicate glass. *NPG Asia Mater.* **11**, 75 (2019).
17. Aoyagi, T., Kohara, S., Naito, T., Onodera, Y., Kodama, M. & Onodera, T. et al. Controlling oxygen coordination and valence of network forming cations. *Sci. Rep.* **10**, 7178 (2020).
18. Waseda, Y. *Novel Application of Anomalous X-ray Scattering for Structural Characterization of Disordered Materials* (Springer, 1984).
19. Waseda, Y. & Sugiyama, K. Structural characterization of non-crystalline oxides by the anomalous X-ray scattering (AXS) method. *High. Temp. Mater. Process.* **22**, 103–121 (2003).
20. Ohara, K., Temleitner, L., Sugimoto, K., Kohara, S., Matsunaga, T. & Pusztai, L. et al. The roles of the Ge–Te core network and the Sb–Te pseudo network during rapid nucleation-dominated crystallization of amorphous $Ge_2Sb_2Te_5$. *Adv. Funct. Mater.* **22**, 2251–2247 (2012).
21. Kohara, S., Tajiri, H., Song, C. H., Ohara, K., Temleitner, L. & Sugimoto, K. et al. Anomalous X-ray scattering studies of functional disordered materials. *J. Phys. Conf. Ser.* **502**, 012014 (2014).
22. Meneghini, C., Gualtieri, A. F. & Siligardi, C. Differential anomalous wide-angle X-ray scattering and X-ray absorption experiments to investigate the formation of glass ceramics in the CaO–$SiO_2$–$ZrO_2$ system. *J. Appl. Cryst.* **32**, 1090–1099 (1999).
23. Arima, H., Kawamata, T. & Sugiyama, K. Local structure around Ge in lithium germanate glasses analyzed by AXS and EXAFS techniques. *J. Miner. Petrol. Sci.* **110**, 60–64 (2015).
24. Ravel, B. & Newville, M. ATHENA, ARTEMIS, HEPHAESTUS: data analysis for X-ray absorption spectroscopy using IFEFFIT. *J. Synchrotron Rad.* **12**, 537–541 (2005).
25. Sakata, O., Furukawa, Y., Goto, S., Mochizuki, T., Uruga, T. & Takeshita, K. et al. Beamline for surface and interface structures at SPring-8. *Surf. Rev. Lett.* **10**, 543–547 (2003).
26. Tajiri, H., Yamazaki, H., Ohashi, H., Goto, S., Sakata, O. & Ishikawa, T. A middle energy-bandwidth X-ray monochromator for high-flux synchrotron diffraction: Revisiting asymmetrically cut silicon crystals. *J. Synchrotron Rad.* **26**, 750–755 (2019).
27. French, B. M., Jezek, P. A. & Appleman, D. E. Virgilite: a new lithium aluminum silicate mineral from the Macusani glass, Peru. *Am. Mineral.* **63**, 461–465 (1978).
28. Bhattacharyya, S. & Höche, T. Direct evidence of Al-rich layers around nano-sized $ZrTiO_4$ in glass: putting the role of nucleation agents in perspective. *Cryst. Growth Des.* **10**, 379–385 (2010).
29. Yokota, R. & Nakajima, H. Small angle X-ray scattering study of spinodal decomposition in $B_2O_3$–PbO–$Al_2O_3$ glass. *J. Non-Cryst. Solids* **70**, 343–357 (1985).
30. Takei, T., Kameshima, Y., Yasumori, A., Okada, K., Kumada, N. & Kinomura, N. SAXS analysis of textures formed by phase separation and crystallization of $Al_2O_3$–$SiO_2$ glasses. *J. Non-Cryst. Solids* **282**, 265–277 (2001).
31. Cahn, J. W. Phase separation by spinodal decomposition in isotropic systems. *J. Chem. Phys.* **42**, 93–99 (1965).
32. Höche, T., Patzig, C., Gemming, T., Wurth, R., Rüssel, C. & Avramov, I. Temporal evolution of diffusion barriers surrounding $ZrTiO_4$ nuclei in lithia aluminosilicate glass-ceramics. *Cryst. Growth Des.* **12**, 1556–1563 (2012).
33. Raghuwanshi, V. S., Rüssel, C. & Hoell, A. Crystallization of $ZrTiO_4$ nanocrystals in lithium-alumino-silicate glass ceramics: anomalous small-angle X-ray scattering investigation. *Cryst. Growth Des.* **14**, 2838–2845 (2014).
34. Chadwick, A. V., Mountjoy, G., Nield, V. M., Poplett, I. J., Smith, M. E. & Strange, J. H. et al. Solid-state NMR and X-ray studies of the structural evolution of nanocrystalline zirconia. *Chem. Mater.* **13**, 1219–1229 (2001).
35. Dura, O. J., Boada, R., López de la Torre, M. A., Aquilanti, G., Rivera-Calzada, A. & Leon, C. et al. XANES and EXAFS study of the local order in nanocrystalline yttria-stabilized zirconia. *Phys. Rev. B* **87**, 174109 (2013).
36. Kleebusch, E., Patzig, C., Krause, M., Hu, Y., Höche, T. & Rüssel, C. The effect of $TiO_2$ on nucleation and crystallization of a $Li_2O$–$Al_2O_3$–$SiO_2$ glass investigated by XANES and STEM. *Sci. Rep.* **8**, 2929 (2018).
37. Kohara, S. & Suzuya, K. Intermediate-range order in vitreous $SiO_2$ and $GeO_2$. *J. Phys. Condens. Matter* **17**, S77–S86 (2005).
38. Kohara, S., Akola, J., Patrikeev, L., Ropo, M., Ohara, K. & Itou, M. et al. Atomic and electronic structures of an extremely fragile liquid. *Nat. Commun.* **5**, 5892 (2014).
39. Hazen, R. M. & Finger, L. W. Crystal structure and compressibility of zircon at high pressure. *Am. Mineral.* **64**, 196–201 (1979).
40. Mozzi, R. L. & Warren, B. E. The structure of vitreous silica. *J. Appl. Cryst.* **2**, 164–172 (1969).
41. Zanotto, E. D. Effect of liquid phase separation on crystal nucleation in glass-formers case closed. *Ceram. Int.* **46**, 24779–24791 (2020).
42. Schmelzer, J. W. P. Crystal nucleation and growth in glass-forming melts: experiment and theory. *J. Non-Cryst. Solids* **354**, 269–278 (2008).